Low-cost micro-supercapacitors using porous Ni/MnO2 entangled pillars and Na-based ionic liquids

Botayna Bounor, Jensheer Shamsudeen Seenath, Sai Gourang Patnaik, David Bourrier, Chau Cam Hoang Tran, Jérôme Esvan, Laurent Weingarten, Armel Descamps-Mandine, Dominic Rochefort, Daniel Guay, et al.

Low-cost micro-supercapacitors based on porous Ni/MnO_2 entangled pillars and Na-based ionic liquids

Botayna Bounor [a], Jensheer Shamsudeen Seenath [a,b], Sai Gourang Patnaik [a], David Bourrier [a], Chau Cam Hoang Tran [a], Jérôme Esvan [c], Laurent Weingarten [d], Armel Descamps-Mandine [d], Dominic Rochefort [b], Daniel Guay [e], David Pech [a,*]

[a] LAAS-CNRS, Université de Toulouse, CNRS, 7 avenue du colonel Roche, Toulouse 31400, France.

[b] Département de chimie, Université de Montréal, 1375 avenue Thérèse-Lavoie-Roux, Montréal, QC H2V 0B3, Canada.

[c] CIRIMAT, Université de Toulouse, CNRS-INPT-UPS, 4 allée Émile Monson, 31400 Toulouse, France.

[d] Centre de Microcaractérisation Raimond Castaing, Université de Toulouse, CNRS, 3 rue Caroline Aigle, 31400 Toulouse, France.

[e] INRS-Énergie, Matériaux et Télécommunications, 1650 Boulevard Lionel Boulet, Varennes, C.P. 1020, Québec J3X 1S2, Canada.

* *E-mail address:* sarinn.pech@cnrs.fr (D. Pech)

Low-cost micro-supercapacitors using porous Ni/MnO_2 entangled pillars and Na-based ionic liquids

Abstract

The enhanced areal energy of three-dimensional (3D) micro-supercapacitors has made these miniaturized energy-storage components increasingly important at the dawn of the Internet of Things. Although ultrahigh-capacitances have been obtained with Ru-based pseudocapacitive materials, their substitution with abundant non-noble transition metals is a key requirement to reduce the price of electrochemical micro-storage systems and enable long-term sustainability. Here we report a cost-effective and industrially feasible approach to realize 3D micro-supercapacitors based on highly porous scaffolds of Ni/MnO_2. These low-price electrodes exhibit a huge areal capacitance exceeding 4 F cm^{-2} and excellent cycling stability. In addition, extended cell voltages up to 2.6 V with areal energy of 1159 mJ cm^{-2} (*i.e.* 0.3 mWh cm^{-2}) and high power of 11.1 mW cm^{-2} were achieved using innovative Na-based ionogel electrolytes. We also show a novel micro-supercapacitor design based on entangled porous Ni/MnO_2 pillars, combining both energy and power ability on a small footprint area.

1. Introduction

The recent development of 3D electrodes based on pseudocapacitive materials [1-4] has greatly reduced the difference between the characteristics of micro-supercapacitors and micro-batteries for embedded systems and on-chip electronics. Small dimension electrochemical energy storage is especially crucial for the upcoming Internet of Things (IoT) based applications, which involve extensive utilization of miniature sensor nodes for health, environmental or industrial monitoring [5,6]. Compared to microbatteries, micro-supercapacitors can provide high-power delivery and, more importantly, have a much longer operating lifetime. This comes, however, at the expense of a much lower energy density.

Pseudocapacitive micro-supercapacitors are a category of electrochemical capacitors whose charge storage mechanism relies on rapid and reversible faradaic surface reactions [7]. When the pseudocapacitive material is deposited as a thin-layer on 3D architectures, high areal energy density is achieved within the limited available space of the electronic circuitry. Using this strategy, we recently reported unprecedented high capacitances per surface area using ruthenium dioxide RuO_2 deposited on porous Au or Pt current collectors [8,9]. These Ru-based micro-supercapacitors deliver an energy density per unit footprint area very close to that of lithium-based microbatteries, but with superior power and better cycling stability [10]. However, the high and volatile price of platinum and ruthenium, as well as the environmental issues related to the mining and refining of these rare and precious metals, have made these micro-devices relegated to niche applications. Replacing ruthenium with alternative transition metals with higher abundance and lower cost is, therefore, fundamental for commercial scale-up.

Among pseudocapacitive materials, manganese dioxide MnO_2 stands out for its high theoretical specific capacitance, wide availability and environmental friendliness [11,12]. Although its capacitance is lower than that of RuO_2, manganese is the fifth most abundant metal in the

Earth's crust making its price derisory compared to the overpriced ruthenium oxide in trace amount. However, MnO_2 suffers from low conductivity, inefficient ion diffusion and a low structural stability, which results in low electrochemical utilization and poor cycling life [13]. We show in this study that the electrodeposition of MnO_2 nanomaterials onto conductive and high surface area Ni foams overcome these issues. The porous metallic structure facilitates electrolyte penetration and enables efficient electronic and ionic pathways resulting in high electrode capacitance. Moreover, the open structure and the nanoscale deposition of MnO_2 in the form of nanoflakes accommodate volume change and mitigate stress upon charge/discharge cycling over long periods of time. Using these inexpensive electrodes along with a cost-effective and scalable manufacturing process, we obtain one of the highest cell capacitances for a micro-supercapacitor device.

2. Materials and Methods

2.1 Elaboration of the electrodes

A thin metallic sublayer (100/200 nm of Ti/Ni) was deposited by evaporation on an oxidized silicon substrate followed by DHBT electrodeposition of porous Ni as current collector with thickness ranging from 144 to 257 μm, using a constant current density of 2 A cm^{-2} in 0.1 M NiCl / 2 M NH_4Cl solution. Pulsed electrodeposition of MnO_2 was afterwards carried out on Ni DHBT in 0.14 M $MnSO_4$ using a potentiostatic pulse of 1.25 V *vs.* SCE (saturated calomel electrode) for 2 s followed by a rest period of 3 s at open circuit potential. The ionic liquids and sodium salts used in this study were purchased from TCI Europe. The electrolytes were prepared in an argon-filled glovebox at room temperature. The electrodes were soaked in the electrolyte overnight prior to electrochemical characterizations.

2.2 Material characterizations

Scanning electron microscopy (SEM) was performed using a Hitachi S-4800 field-emission microscope. Transmission electron microscopy (TEM) imaging was carried out using a JEOL 2100F microscope equipped with a Schottky field emission gun (FEG) operated at 200 kV and a Gatan RIO16IS CMOS camera. The TEM sample was prepared using an epoxy resin for hardening before mechanical thinning (SiC polishing cloth and concave polishing using a diamond suspension) and final finishing by ion beam. The crystallographic structures were analyzed by grazing incidence X-ray diffraction (GI-XRD) measurements on a Bruker D8 advanced X-ray diffractometer with Cu K_α radiation (1.54184 Å) operating at 40 kV and 40 mA. The surface chemical composition of manganese oxide was estimated via X-ray photoelectron spectroscopy (XPS) using a ThermoScientific K-Alpha system operating with a monochromatic Al K_α X- ray source (1486.6 eV). The spectrometer energy was calibrated using the Au $4f_{7/2}$ (83.9 ± 0.1 eV) and Cu $2p_{3/2}$ (932.8 ± 0.1 eV) photoelectron lines.

2.3 Electrochemical characterizations

The electrochemical synthesis and characterizations were performed with a VMP-3 Biologic potentiostat connected to an external 10 A booster channel. The three-electrode system was made up of the working electrode, a Pt mesh counter electrode, a saturated calomel electrode (SCE) for synthesis and a KCl saturated Ag/AgCl reference electrode for characterizations. Electrochemical impedance spectroscopy (EIS) measurements were carried out at open circuit potential and frequencies ranging from 100 kHz to 10 mHz.

The accessibility of charges has been investigated by calculating the voltammetric charge, q^*, as a function of the sweep rate, v. The outer charge, q_o, is obtained from the extrapolation of q^* when $v \rightarrow \infty$ from the $q^* = f(1/v^{1/2})$ plot. The total charge, q_t, is determined using the extrapolation of the inverse of the voltammetric charge, $1/q^*$, when $v \rightarrow 0$ from the $1/q^* = f(v^{1/2})$ plot.

2.4 AEF factor calculation of Ni scaffolds

The Area Enlargement Factor (*AEF*) of the metallic current collector was defined as follows:

$$AEF = \frac{Electrochemical\ Active\ Surface\ Area\ (EASA)}{Geometrical\ Area}$$

The *EASA* of porous Ni DHBT coatings was calculated by integrating the charge associated to the β-NiOOH → β-$Ni(OH)_2$ reduction peak using cyclic voltammetry at 5 mV s^{-1} in 1 M KOH, considering a cathodic charge value of 2.1 mC cm^{-2} as a reference [14,15].

3. Results and Discussion

3.1 Porous Ni/MnO_2 electrodes

Highly porous Ni current collectors were synthesized by a facile and scalable electrodeposition process on oxidized Si wafers: the dynamic hydrogen bubble template (DHBT) method [16]. In this process, the electrodeposition of the metallic material from aqueous solutions is performed at high cathodic overpotentials where H^+ is reduced to H_2. The generation of hydrogen gas bubbles acts as a dynamic template for the growth of highly porous metal films interspersed with nanostructured pore walls. This synthesis method is very simple and provide porous structures with good mechanical stability and strong adherence to the substrate. Moreover, compared to other procedures based on stationary physical templates [17,18], DHBT process does not require any subsequent etching or template removal step, thus reducing post-processing and associated difficulties or compatibility.

An Area Enlargement Factor (*AEF*), defined as the ratio between the developed area of the Ni porous structure over its projected area, can be deduced from cyclic voltammograms (CVs) in alkaline media (see Materials and Methods section). Fig. 1a shows the evolution of the CVs and corresponding calculated *AEF* of different porous Ni foams obtained with increasing DHBT deposition times. As expected, the *AEF* increases steadily with the deposition duration and

hence the film thickness, from 342 cm^2 cm^{-2} to a colossal *AEF* value of about 1000 cm^2 cm^{-2} for 30 min of deposition. The formed metal foams are composed primarily of polycrystalline Ni as confirmed from their X-ray diffraction (XRD) pattern (Fig. 1b). The scanning electron micrographs (SEM) (Fig. 1b inset) show porous surface structure with different pore sizes, with diameters varying between 10 and 50 μm for the largest. Individual pores are constructed with converging nanoscale spicule-like structures, thus providing enormous surface area.

We then electrodeposited the MnO_2 as active material using a pulsed current technique on the highly structured nickel current collector (Figure S1). From cross-sectional SEM observations (Figure S2), the electrodes display a pine tree type morphology with uniformly spread active material. High resolution transmission electron microscopy (TEM) imaging (Figure S3) and fast Fourier transform (FFT) analysis (Figure S4) show continuous and uniform deposition of ultra-small nanoflakes with ~77 nm thickness, with interplanar spacings characteristic of ramsdellite phase of the 1D allotropic group of MnO_2 [19]. The elemental mapping images (Fig. 2a) further illustrate the homogeneous distribution and coverage of Mn on the Ni metal support with unfilled open pores/space for electrolyte penetration. The composition of deposited MnO_2 was also confirmed through X-ray photoelectron spectroscopy (XPS) studies by tracking the peak splitting difference of Mn-3s states at electrochemically reduced (0 V *vs.* Ag/AgCl) and oxidized (0.9 V *vs.* Ag/AgCl) forms (Fig. 2b). The exchange-splitting of the 3s core levels results in a binding energy separation directly related to the valence of manganese and its average oxidation state in the oxide, with a negative linear relationship [20]. The energy splitting of the Mn-3s core level peaks is 4.9 eV for the as-deposited material, and 4.7 eV after oxidation, which is consistent with the occurrence of a MnO_2 phase in a Mn(IV) oxidation state [21]. This high Mn(IV) content is also in agreement with the quantitative determination computed from the Mn-$2p_{3/2}$ and O-1s core level spectra (Figure S5). In its fully reduced state (Mn^{3+}), the binding energy difference of the Mn-3s core level peaks should be ~5.4 eV, but in

the current case, the peak separation in the reduced state was ~5.1 eV, suggesting incomplete reduction at 0 V. These XPS results are nevertheless in accordance with the established pseudocapacitance reaction based on the change of oxidation state varying between Mn(IV) and Mn(III) with one-electron transfer in neutral aqueous medium [22].

Electrochemical characterizations of the porous Ni/MnO_2 electrode (25 min of Ni DHBT and 1500 pulses of MnO_2 electrodeposition) were performed in a three-electrode configuration in a nitrogen-purged 1 M Na_2SO_4 aqueous electrolyte. Fig. 2c shows the obtained electrochemical impedance spectroscopy (EIS) measurements along with the simulated fit using a classical equivalent circuit model to distinguish pseudocapacitance from double-layer capacitance. The composite electrode is characterized by a low equivalent series resistance (ESR) of 7.0 Ω cm^2 indicating small internal electrical resistance and energy loss. The cyclic voltammograms, recorded at different scan rates, show an almost ideal symmetrical rectangular shape (Fig. 2d), revealing easy and efficient access of electrons and cations to the pseudocapacitive 3D electrode to afford fast and highly reversible redox reactions. More importantly, the electrode exhibits a huge areal capacitance of 1.8 F cm^{-2} when cycled at 0.1 mV s^{-1} and 2.9 F cm^{-2} at 10 mHz using EIS (Fig. 2c), which is by far higher than all reported 2D thin-film micro-supercapacitor electrodes [5,23-25].

The accessibility of the electrolyte to the electroactive material has been further investigated by calculating the voltammetric charge, q^*, as a function of the sweep rates, v, from 0.1 to 20 mV s^{-1} (Fig. 2e) according to a procedure developed by Trasatti and co-workers [26]. This advanced electrochemical data analysis has been performed for Na^+ storage on different samples with increasing number of electrodeposited cycles of MnO_2 (Fig. 2f). The difference between the outer capacitance, C_o, related to the most accessible $Mn^{3+/4+}$ sites at the surface of the MnO_2 deposits, and the total capacitance, C_t, gradually increases with deposition cycles indicating that accessibility of active surface area becomes progressively more and more

difficult. Indeed, the reaction mechanism involves an adsorption/desorption process of Na^+ at the surface of MnO_2 flakes as well as an insertion/extraction of the alkali ion into the bulk of the material. However, even for the thicker MnO_2 coating obtained after 2500 cycles of deposition, the main contribution of the total capacitance C_t comes from the outer capacitance C_o, which accounts for 69 % of the total capacitance, depicting the effectiveness of the porous matrix in enabling a large part of the nanostructured MnO_2 film to be electrochemically active. The value C_t reaches 4.0 F cm^{-2} (*i.e.* ~110 F g^{-1}, as expected for gravimetric capacitance of ramsdellite[19]) for the sample with the highest active material loading. This is the highest capacitance per unit area ever reported for 3D MnO_2 micro-supercapacitor electrodes [27-31]. In order to verify whether the DHBT structure can provide a reliable electrical connection to the inherently poorly conductive MnO_2, the long-term behavior of the electrode was tested by repeated galvanostatic charge/discharge cycles at high current of 4 mA cm^{-2} (Fig. 2g). The cycling experiment indicates excellent stability of the composite porous electrodes with more than 80 % retention of the initial capacitance after 10 000 cycles, and SEM images after cycling tests show that morphology of the MnO_2 is preserved (Figure S6). This impressive stability of nanocrystalline MnO_2 when extra-long measurements are performed can be explained by the conductive and porous structure of the metallic current collector as well as the beneficial effect of nanosizing on transport properties which govern the electrode reversibility [32]. Moreover, unlike 2D thick-film electrodes, delamination issue is not a concern for these binder and additive-free structures.

3.2 Cell performances

Motivated by the excellent capacitive performance of porous Ni/MnO_2 architectures in three-electrode configuration, their integration and functioning in full-cell microdevices were subsequently examined. The realization of a 3D configuration at the device-level integrating

nanostructured electrodes is an important milestone to further improve the surface-to-volume ratio and obtain the desired combination of energy, power, lifetime on small footprint areas [33]. While the interdigitated planar configuration can shorten the diffusion length between the positive and negative electrode [34], a better areal capacitance and energy can be achieved for a micro-supercapacitor in stack configuration [5]. We provide here an innovative framework to realize three-dimensional micro-supercapacitors consisting of entangled pillars of porous Ni/MnO_2, as schematically shown in Fig. 3a,b. The microfabrication steps are detailed in Figure S7 and assembling details in Figure S8. The principle is based on the electrodeposition of Ni pillars inside photoresist molds, followed by DHBT electrodeposition of porous Ni and electrodeposition of MnO_2. This new concept of 3D device design combines both the advantages of the interdigitated and the ones of the stack configuration, with reduced interelectrode distance and increased active material loading over limited surface area. This arranged matrix of 3D porous electrodes also facilitates better electrolyte percolation and higher electronic conductivity, thus resulting in superior interfacial kinetics. The entire process of fabrication is easily scalable (Figure S9) thanks to the simplicity of the DHBT template, and can be used with pillars of different geometries (square, hexagonal, parallelogram or spinner as shown in Figure S10) to maximize their density per unit area (see Table S1 for example). Important to note here is that this general scheme of construction can be easily extended to other class of substrates since the fabrication process is facile and needs thin metallic films, from which porous Ni foams can be grown through aqueous electrodeposition.

Fig. 3c shows the cyclic voltammograms in 1 M Na_2SO_4 of a 15 mm^2 micro-supercapacitor cell based on 179 μm thick porous Ni/MnO_2 electrodes. The Ni/MnO_2 micro-device exhibits a remarkable cell capacitance of 846 mF cm^{-2} at 1 mV s^{-1}, which is the highest value ever reported for a full-cell micro-supercapacitor [1,17,31,35-38] including those based on 3D Ru oxides [8]. Moreover, the CV profiles did not show resistive behavior even at high scan rate of 50 mV s^{-1}.

3.3 MnO_2 micro-supercapacitor based on Na-based ionic liquids

The use of aqueous electrolyte restricted the operating voltage range because of water decomposition and partial dissolution of MnO_2 into soluble MnOOH species above *ca.* 1 volt. The development of advanced solid-state electrolytes suitable for Na^+ charge storage with extended electrochemical stability window (ESW) is therefore an important challenge as energy stored is directly proportional to the square of the cell voltage. We have demonstrated in previous studies that a high pseudocapacitive effect of RuO_2 with extended ESW could be obtained using protic ionic liquids [39,40]. Herein, we have synthesized and tested various innovative electrolytes using Na salts diluted in aprotic pyrrolidinium- and imidazolium-based ionic liquids solvents for MnO_2. Figure S11 shows the structure of the different ionic liquids explored and Figure S12 their electrochemical behaviour with Ni/MnO_2 electrodes. Ionic liquids are considered safe alternatives to conventional aqueous and organic electrolytes due to their non-flammability, low volatility, high ionic conductivity and widened potential windows. Moreover, ionic liquids can be easily turned into quasi-solid state by the use of ionogels [41,42] and address the packaging issues of micro-supercapacitors.

We tested the micro-device using 1 M sodium bis(fluorosulfonyl)imide (NaFSI) salt diluted in aprotic 1-methyl-1-propylpyrrolidinium bis(fluorosulfonyl)imide ($Pyr_{13}FSI$) ionic liquid (Fig. 3d), where Na^+ ion can be expected to be the dominant contributor to faradaic pseudocapacitance [43] and greatly enhances charge storage [44,45]. Ionic liquid based on FSI^- anions are known to be chemically stable and to provide relative low viscosity [46,47], which often correlates with good ionic conduction. CVs were performed at 2 mV s^{-1} with increasing cell voltage windows. To our surprise, the micro-supercapacitor was able to cycle up to 2.6 V with no oxidation peaks that would be related to active material degradation. The voltammetric charge/discharge ratio of Figure S13 also reveals an appreciable level of stability over this

voltage range. This wide extension of cell voltage could suggest that manganese oxide pseudocapacitance may rely on oxidation states above +IV using stable ionic liquids, with more than one-electron transfer, according to the following reaction:

$$Mn^{n+}O_{n/2} + (n-3)Na^{+} + (n-3)e^{-} \leftrightarrow Na^{+}_{(n-3)}Mn^{3+}O_{n/2} \quad (1)$$

where $n \geq 4$ is the maximum oxidation number of Mn.

Mn has indeed stable oxidation states, ranging from +2 to +7, in different known oxides [48,49]. A significant portion of the stored energy could also come from the electrochemical double-layer capacitance (EDLC) of aprotic $Pyr_{13}FSI$ solvent with the highly porous structure. Moreover, earlier studies on MnO_2 supercapacitors using neat ionic liquids without added salts have shown that small anions can intercalate into the structure to support faradaic charge storage [50]. Although this high voltage comes at the expense of a lower cell capacitance (343 mF cm^{-2}), the specific energy reaches in this case an outstanding value of 1159 mJ cm^{-2} (*i.e.* 0.3 mWh cm^{-2}).

Fig. 3e and Figure S14 show the cycling performance of micro-supercapacitor prototypes up to 2000 cycles in various ionic liquid-based media. Using NaFSI/$Pyr_{13}FSI$, a slight increase of capacitance is observed at the beginning of cycling ascribed to a gradual penetration of the electrolyte within the porosity, followed by a very high stability, pointing out the reliability of the microdevices on long cycles. The overall performances of the cells are finally compared with state-of-the-art reports on micro-supercapacitors in an area-normalized Ragone plot (Fig. 4 and Table S2) [17,23,37,51-54]. Our economical aqueous MnO_2 microdevice rivals the best reported RuO_2 micro-supercapacitor while the ionic liquid-based one outperforms it.

4. Conclusion

We have demonstrated the possibility of realizing low-cost micro-supercapacitor MnO_2-based electrodes having ultra-long lifetimes and areal capacitances competing with the archetypal

pseudocapacitive RuO_2. Furthermore, these performances can be easily improved by increasing the depth of the 3D scaffold and tuning the MnO_x thickness accordingly. We also lay down general scheme of microfabrication process to construct full encapsulated devices that could be easily extended to other substrates and geometric shapes/forms. The entire technological process is cost-effective, environmentally friendly, with all processing steps performed at room temperature, from the electrodeposition of Ni DHBT and MnO_2 active material to wafer-level integration of the micro-devices. To enable extended operational potential window, we have screened various ionic liquid-based media and show prototype cells with optimized electrolyte having superlative performance. Each of the sub-components of the final device is tailored to be economically feasible for scale up, thus opening avenues for successful commercialization.

Acknowledgements

The authors acknowledge the support from the European Research Council (ERC Consolidator Grant, ERC-2017-CoG, project 771793 3D-CAP and ERC Proof-of-Concept, ERC-2022-PoC, project 101069259 3D-APP). This work was supported by LAAS-CNRS technology platform, a member of Renatech network.

References

1. S. Zheng, X. Shi, P. Das, Z.-S. Wu, X. Bao, The road towards planar microbatteries and micro-supercapacitors: from 2D to 3D device geometries, Adv. Mater. 31 (2019) 1900583.

2. M. Sha, H. Zhao, Y. Lei, Updated insights into 3D architecture electrodes for micropower sources, Adv. Mater. 33 (2021) 2103304.

3. C. Li, X. Li, Q. Yang, P. Sun, L. Wu, B. Nie, H. Tian, Y. Wang, C. Wang, X. Chen, J. Shao, Tuning the mechanical and electrical properties of porous electrodes for architecting 3D microsupercapacitors with batteries-level energy, Adv. Sci. 8 (2021) 2004957.

4. P. Zhang, S. Yang, H. Xie, Y. Li, F. Wang, M. Gao, K. Guo, R. Wang, X. Lu, Advanced three-dimensional microelectrode architecture design for high-performance on-chip micro-supercapacitors, ACS Nano 16 (2022) 17593-17612.

5. N.A. Kyerematen, T. Brousse, D. Pech, Microsupercapacitors as miniaturized energy-storage components for on-chip electronics, Nat. Nanotechnol. 12 (2017) 7-15.

6. J.H. Pikul, H. Ning, Powering the Internet of Things, Joule 2 (2018) 1036-1038.

7. S. Fleischmann, J.B. Mitchell, R. Wang, C. Zhang, D. Jiang, V. Presser, V. Augustyn, Pseudocapacitance: from fundamental understanding to high power energy storage materials, Chem. Rev. 120 (2020) 6738-6782.

8. S.G. Patnaik, J.S. Seenath, D. Bourrier, S. Prabhudev, D. Guay, D. Pech, Porous $RuO_xN_yS_z$ electrodes for microsupercapacitors and microbatteries with enhanced areal performance, ACS Energy Lett. 6 (2021) 131-139.

9. L.B. Karroubi, S.G. Patnaik, B.D. Assresahegn, B. Bounor, C.C.H. Tran, S.H. Choudhury, D. Bourrier, D. Guay, D. Pech, Highly porous scaffolds for Ru-based microsupercapacitor electrodes using hydrogen bubble templated electrodeposition, Energy Storage Mater. 47 (2022) 134-140.

10. A. Ferris, S. Garbarino, D. Guay, D. Pech, 3D RuO_2 microsupercapacitors with remarkable areal energy, Adv. Mater. 27 (2015) 6625-6629.

11. W. Wei, X. Cui, W. Chen, D.G. Ivey, Manganese oxide-based materials as electrochemical supercapacitor electrodes, Chem. Soc. Rec. 40 (2011) 1697-1721.

12. S. Boyd, K. Ganeshan, W.-Y. Tsai, T. Wu, S. Saeed, D. Jiang, N. Balke, A.C.T. van Duin, V. Augustyn, Effects of interlayer confinement and hydration on capacitive charge storage in birnessite, Nat. Mater. 20 (2021) 1689-1694.

13. Y.-C. Hsieh, K.-T. Lee, Y.-P. Lin, N.-L. Wu, S.W. Donne, Investigation on capacity fading of aqueous $MnO_2.nH_2O$ electrochemical capacitor, J. Power Sources 177 (2008) 660-664.

14. M. Hao, V. Charbonneau, N.N. Fomena, J. Gaudet, D.R. Bruce, S. Garbarino, D.A. Harrington, D. Guay, Hydrogen bubble templating of fractal Ni catalysts for water oxidation in alkaline media, ACS Appl. Energy Mater. 2 (2019) 5734-5743.

15. E. Cossar, M.S.E. Houache, Z. Zhang, E.A. Baranova, Comparison of electrochemical active surface area methods for various nickel nanostructures, J. Electroanal. Chem. 870 (2020) 114246.

16. B.J. Plowman, L.A. Jones, S.K. Bhargava, Building with bubbles: the formation of high surface area honeycomb-like films via hydrogen bubble templated electrodeposition, Chem. Commun. 51 (2015) 4331-4346.

17. E. Eustache, C. Douard, A. Demortière, V. De Andrade, M. Brachet, J. Le Bideau, T. Brousse, C. Lethien, High areal energy 3D-interdigitated micro-supercapacitors in aqueous and ionic liquid electrolytes, Adv. Mater. Technol. 2 (2017) 1700126.

18. L. Wen, R. Xu, Y. Mi, Y. Lei, Multiple nanostructures based on anodized aluminium oxide templates, Nat. Nanotechnol. 2017, 12, 244-250.

19. O. Ghodbane, J.L. Pascal, F. Favier, Microstructural effects on charge-storage properties in MnO_2-based electrochemical supercapacitors, ACS Appl. Mater. Interfaces 1 (2009) 1130-1139.

20. M. Toupin, T. Brousse, D. Bélanger, Influence of microstructure on the charge storage properties of chemically synthesized manganese dioxide, Chem. Mater. 14 (2002) 3946-3952.

21. A. Audi, P. Sherwood, Valence-band x-ray photoelectron spectroscopic studies of manganese and its oxides interpreted by cluster and band structure calculations, Surf. Interface Anal. 33 (2002) 274-282.

22. T. Brousse, M. Toupin, R. Dugas, L. Athouël, O. Crosnier, D. Bélanger, Crystalline MnO_2 as possible alternatives to amorphous compounds in electrochemical capacitors, J. Electrochem. Soc. 153 (2006) A2171-A2180.

23. P. Huang, C. Lethien, S. Pinaud, K. Brousse, R. Laloo, V. Turq, M. Respaud, A. Demortière, B. Daffos, P.-L. Taberna, B. Chaudret, Y. Gogotsi, P. Simon, On-chip and freestanding elastic carbon films for micro-supercapacitors, Science 351 (2016) 691-695.

24. F. Bu, W. Zhou, Y. Xu, Y. Du, C. Guan, W. Huang, Recent developments of advanced micro-supercapacitors: design, fabrication and applications, npj Flex. Electron. 4 (2020) 31.

25. A. Jrondi, G. Buvat, F. De La Pena, M. Marinova, M. Huvé, T. Brousse, P. Roussel, C. Lethien, Major improvement in the cycling ability of pseudocapacitive vanadium nitride films for micro-supercapacitor, Adv. Energy Mater. 13 (2023) 2203462.

26. S. Ardizzone, G. Fregonara, S. Trasatti, “Inner” and “outer” active surface of RuO_2 electrodes, Electrochim. Acta 35 (1990) 263-267.

27. E. Eustache, C. Douard, R. Retoux, C. Lethien, T. Brousse, MnO_2 thin films on 3D scaffold: microsupercapacitor electrodes competing with “bulk” carbon electrodes, Adv. Energy Mater. 5 (2015) 1500680.

28. M.F. El-Kady, M. Ihns, M. Li, J.Y. Hwang, M.F. Mousavi, L. Chaney, A.T. Lech, R.B. Kaner, Engineering three-dimensional hybrid supercapacitors and microsupercapacitors for high-performance integrated energy storage, Proc. Natl. Acad. Sci. USA 112 (2015) 4233-4238.

29. H. Hu, Z. Pei, H. Fan, C. Ye, 3D interdigital Au/MnO_2/Au stacked hybrid electrodes for on-chip microsupercapacitors, Small 12 (2016) 3059-3069.

30. Y. Wang, L. Sun, D. Xiao, H. Du, Z. Yang, X. Wang, L. Tu, C. Zhao, F. Hu, B. Lu, Silicon-based 3D all-solid-state microsupercapacitor with superior performance, ACS Appl. Mater. Interfaces 12 (2020) 43864-43875.

31. B. Bounor, B. Asbani, C. Douard, F. Favier, T. Brousse, C. Lethien, On chip MnO_2-based 3D micro-supercapacitors with ultra-high areal energy density, Energy Storage Mater. 38 (2021) 520-527.

32. C.M. Julien and A. Mauger, Nanostructured MnO_2 as electrode materials for energy storage, Nanomaterials 7 (2017) 396.

33. L. Liu, H. Zhao, Y. Lei, Advances on three-dimensional electrodes for micro-supercapacitors: a mini-review, InfoMat 1 (2019) 74-84.

34. D. Pech, M. Brunet, T.M. Dinh, K. Armstrong, J. Gaudet, D. Guay, Influence of the configuration in planar interdigitated electrochemical micro-capacitors, J. Power Sources 230 (2013) 230-235.

35. K. Brousse, S. Pinaud, S. Nguyen, P.-F. Fazzini, R. Makarem, C. Josse, Y. Thimont, B. Chaudret, P.-L. Taberna, M. Respaud, P. Simon, Facile and scalable preparation of ruthenium oxide-based flexible micro-supercapacitors, Adv. Energy Mater. 10 (2020) 1903136.

36. C. Gao, J. Huang, Y. Xiao, G. Zhang, C. Dai, Z. Li, Y. Zhao, L. Jiang, L. Qu, A seamlessly integrated device of micro-supercapacitor and wireless charging with ultrahigh energy density and capacitance, Nat. Commun. 12 (2021) 2647.

37. P. Zhang, Biomimetic platinum forest enables 3D micro-supercapacitors with enhanced areal performance, Chem. Eng. J. 454 (2023) 140357.

38. A. Sajedi-Moghaddam, M. Gholami, N. Naseri, Inkjet printing of MnO_2 nanoflowers on surface-modified A4 paper for flexible all-solid-state microsupercapacitors, ACS Appl. Mater. Interfaces 15 (2023) 3894-3903.

39. D. Rochefort, A.L. Pont, Pseudocapacitive behaviour of RuO_2 in a proton exchange ionic liquid, Electrochem. Commun. 8 (2006) 1539-1543.

40. J.S. Seenath, D. Pech, D. Rochefort, Investigation of protic ionic liquid electrolytes for porous RuO_2 micro-supercapacitors, J. Power Sources 548 (2022) 232040.

41. J. Le Bideau, L. Viau, A. Vioux, Ionogels, ionic liquids based hybrid materials, Chem. Soc. Rev. 40 (2011) 907-925.

42. T. Guillemin, C. Douard, K. Robert, B. Asbani, C. Lethien, T. Brousse, J. Le Bideau, Solid-state 3D micro-supercapacitors based on ionogel electrolyte: influence of adding lithium and sodium salts to the ionic liquid, Energy Storage Mater. 50 (2022) 606-617.

43. S. Lindberg, S. Jeschke, P. Jankowski, M. Abdelhamid, T. Brousse, J. Le Bideau, P. Johansson, A. Matic, Charge storage mechanism of α-MnO_2 in protic and aprotic ionic liquid electrolytes, J. Power Sources 460 (2020) 228111.

44. Y.S. Li, I.-W. Sun, J.-K. Chang, C.-J. Su, M.T. Lee, Doped butylmethylpyrrolidinium-dicyanamide ionic liquid as an electrolyte for MnO_2 supercapacitors, J. Mater. Chem. 22 (2012) 6274-6279.

45. T.M. Benedetti, V.R. Gonçales, S.I. Córdoba de Torresi, R.M. Torresi, In search of an appropriate ionic liquid as electrolyte for microporous manganese oxide film electrochemistry, J. Power Sources 239 (2013) 1-8.

46. I.A. Shkrob, T.W. Marin, Y. Zhu, D.P. Abraham, Why bis(fluorosulfonyl)imide is a "magic anion" for electrochemistry, J. Phys. Chem. C 118 (2014) 19661-19671.

47. M. Kerner, N. Plylahan, P. Johansson, Ionic liquid based lithium battery electrolytes: fundamentals benefits of utilising both TFSI and FSI anions?, Phys. Chem. Chem. Phys. 17 (2015) 19569-19581.

48. M.-K. Song, S. Sheng, H. Chen, W. Qin, K.-W. Nam, S. Xu, X.-Q. Yang, A. Bongiorno, J. Lee, J. Bai, T.A. Tyson, J. Cho, M. Liu, Anomalous pseudocapacitance behavior of a nanostructured, mixed-valent manganese oxide film for electrical energy storage, Nano Lett. 12 (2012) 3483-3490.

49. S.K. Ghosh, Diversity in the family of manganese oxides at the nanoscale: from fundamentals to applications, ACS Omega 5 (2020) 25493-25504.

50. J.-K. Chang, M.-T. Lee, W.-T. Tsai, M.-J. Deng, I.-W. Sun, X-ray photoelectron spectroscopy and in situ X-ray absorption spectroscopy studies on reversible insertion/desertion of dicyanamide anions into/from manganese oxide in ionic liquid, Chem. Mater. 21 (2009) 2688-2695.

51. D. Pech, M. Brunet, H. Durou, P. Huang, V. Mochalin, Y. Gogotsi, P.-L. Taberna, P. Simon, Ultrahigh-power micrometre-sized supercapacitors based on onion-like carbon, Nat. Nanotechnol. 5 (2010) 651-654.

52. J. Lin, Z. Peng, Y. Liu, F. Ruiz-Zepeda, R. Ye, E.L.G. Samuel, M.J. Yacaman, B.I. Yakobson, J.M. Tour, Laser-induced porous graphene films from commercial polymers, Nat. Commun. 5 (2014) 5714.

53. K. Robert, C. Douard, A. Demortière, F. Blanchard, P. Roussel, T. Brousse, C. Lethien, On chip interdigitated micro-supercapacitors based on sputtered bifunctional vanadium nitride thin films with finely tuned inter- and intracolumnar porosities, Adv. Mater. Technol. 3 (2018) 1800036.

54. A. Ferris, D. Bourrier, S. Garbarino, D. Guay, D. Pech, 3D interdigitated microsupercapacitors with record areal cell capacitance, Small 15 (2019) 1901224.

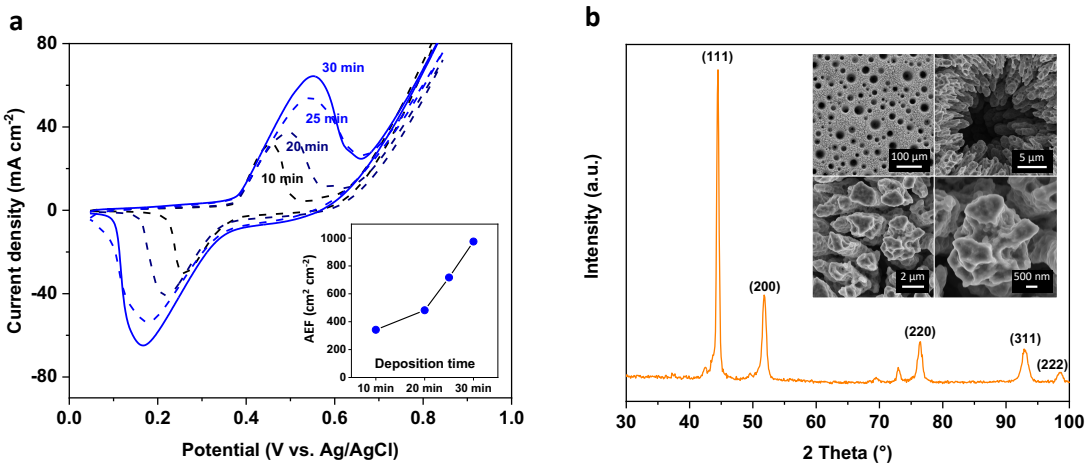

Fig. 1. Characterizations of Ni porous current collectors. a) Evolution of the Area Enlargement Factor (AEF), deduced from CVs performed at 5 mV s^{-1} in 1 M KOH, with DHBT deposition time. Large AEF up to *ca.* 1000 cm^2 cm^{-2} were obtained. b) XRD pattern showing the diffraction peaks of Ni and SEM images at different magnifications.

Figure 1

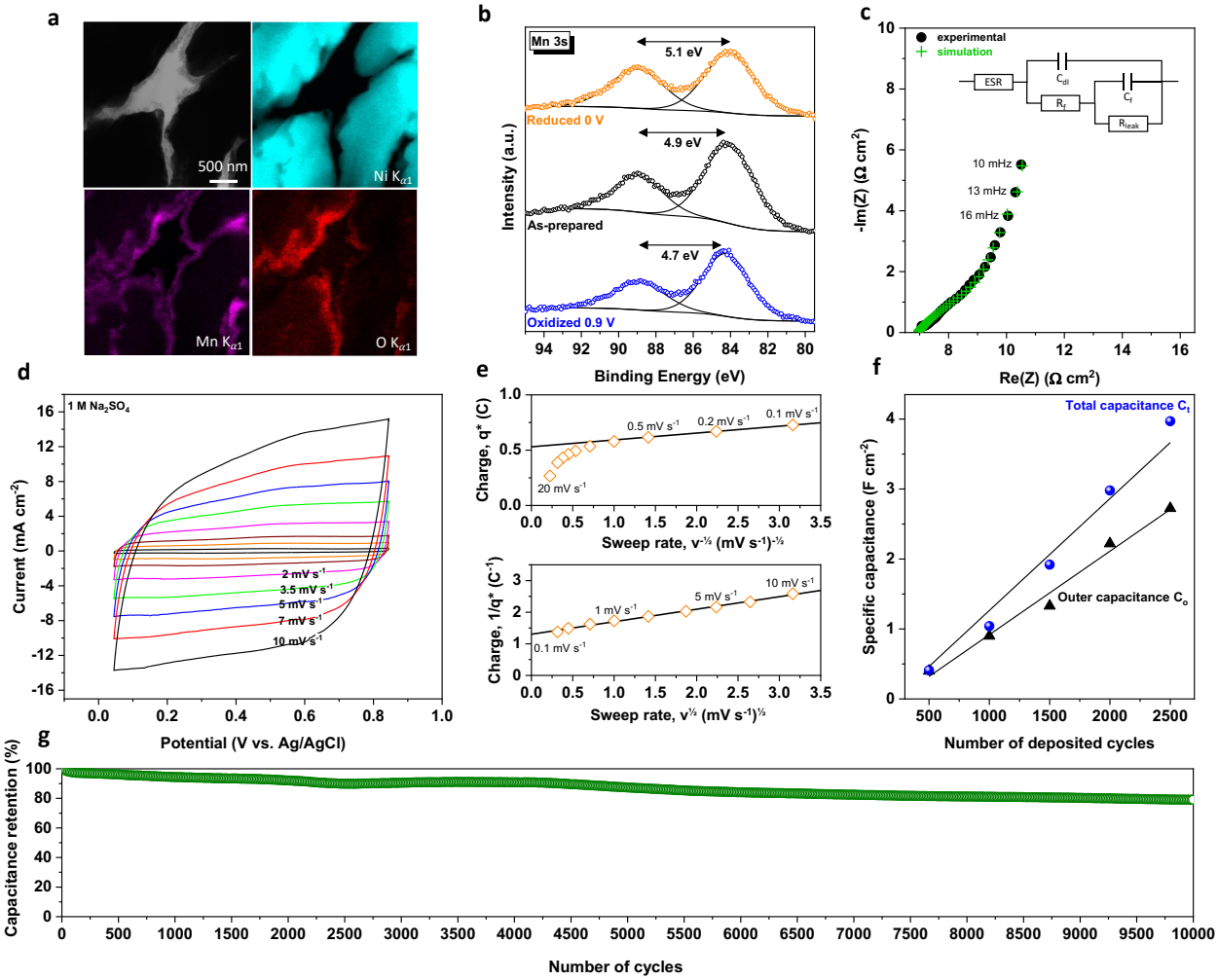

Fig. 2. Characterizations of porous Ni/MnO_2 electrodes (25 min Ni DHBT + 1500 pulses of MnO_2). a) TEM image and elemental mapping showing a uniform deposition of MnO_2 into the porous Ni current collectors. b) Peak splitting difference of the Mn-3s core-level XPS spectrum of the Ni/MnO_2 electrode reduced at 0 V and oxidized at 0.9 V *vs.* Ag/AgCl in 1 M Na_2SO_4. c) Experimental and simulated Nyquist plot. d) Cyclic voltammetry profiles from 0.1 to 10 mV s^{-1}. e) Determination of the outer charge, q_o, and total charge, q_t, obtained by calculating the voltammetric charge q^* as a function of the sweep rate v. f) Evolution of outer capacitance, C_o, and total capacitance, C_t, with the number of MnO_2 electrodeposition cycles. g) Stability of the electrode during long-term galvanostatic charge-discharge cycles at 4 mA cm^{-2}.

Figure 2

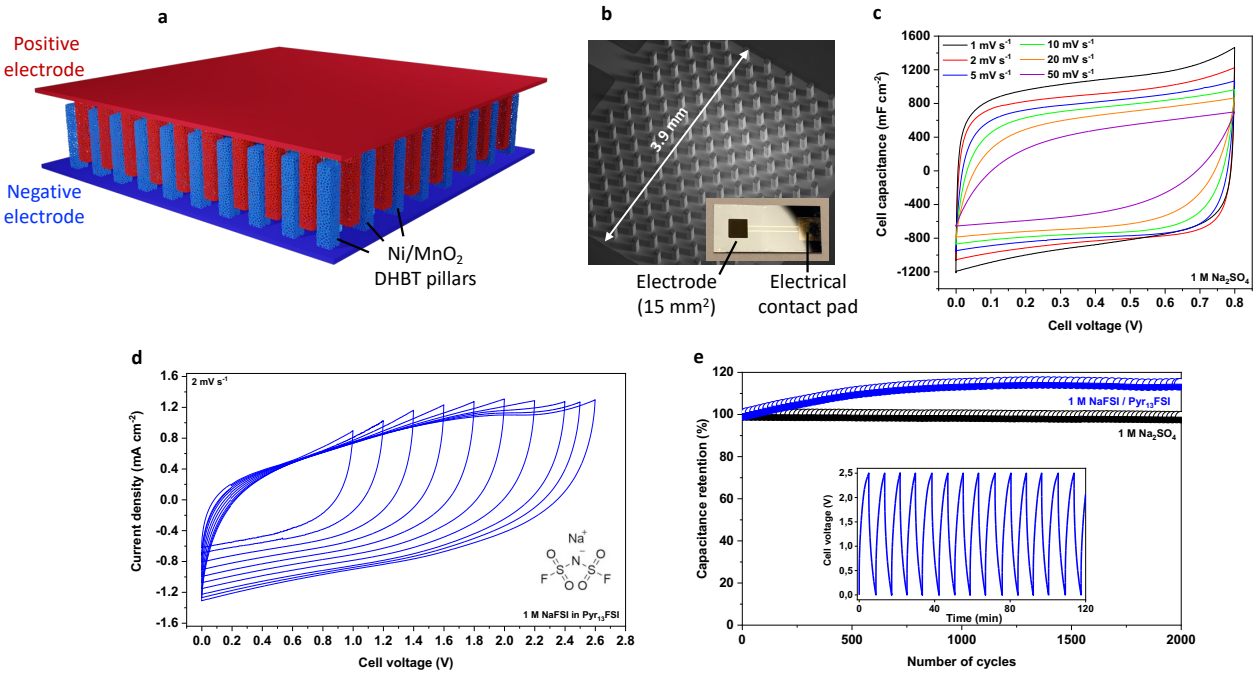

Fig. 3. Cell performances. a) Illustration of a 3D stacked micro-supercapacitor design (symmetric configuration). b) SEM and optical image of one 3D electrode before stacking and encapsulation. c) Evolution of stack capacitance with increasing scan rate in 1 M Na_2SO_4. d) Cell voltage increase in 1 M NaFSI /Pyr_{13}FSI ionic liquid. e) Cell capacitance retention with increasing number of charge/discharge cycles (2 mA cm^{-2}) of a 15 mm^2 encapsulated prototype using 1 M Na_2SO_4 /H_2O and 1 M NaFSI /Pyr_{13}FSI electrolyte.

Figure 3

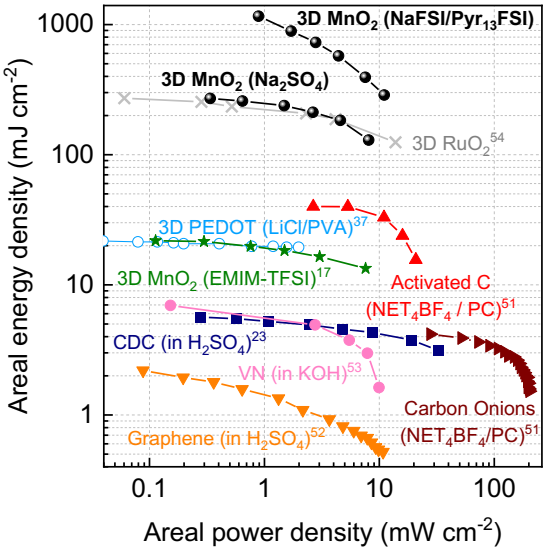

CDC, carbide-derived carbon; NEt_4BF_4, tetraethylammonium tetrafluoroborate; PC, propylene carbonate; PEDOT, poly(3,4-ethylenedioxythiophene; PVA, polyvinyl alcohol; EMIM-TFSI, 1-ethyl-3-methylimidazolium bis(trifluoromethylsulfonyl)imide.

Fig. 4. Comparison with state-of-the-art micro-supercapacitors. Ragone plot showing the specific energy and power per surface area of supercapacitor microdevices based on several active materials.

Supplementary Material

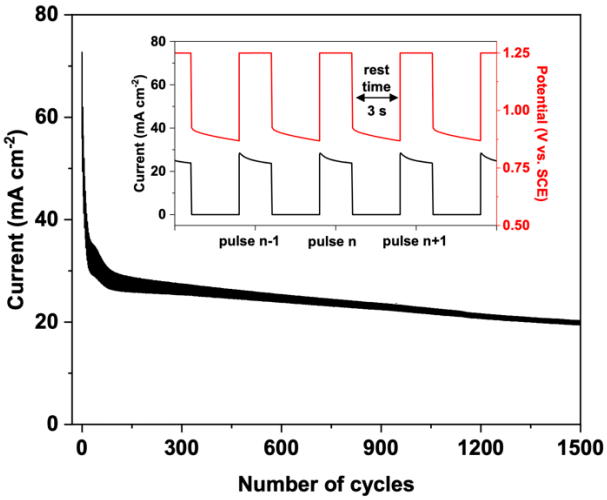

Figure S1. Potentiostatic pulsed electrodeposition of MnO_2 on porous Ni current collectors. Each cycle consists of a potentiostatic pulse of 1.25 *vs.* SCE for 2 s followed by a rest period of 3 s at open circuit to stabilize the porous/electrolyte interface.

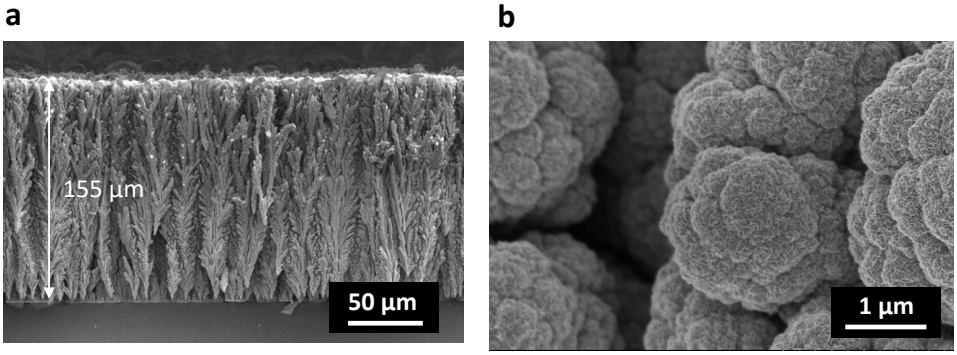

Figure S2. Cross-sectional SEM image of a Ni DHBT/MnO_2 electrode. a) Low magnification. b) High magnification showing uniform deposition of MnO_2 active material.

Supplementary Material

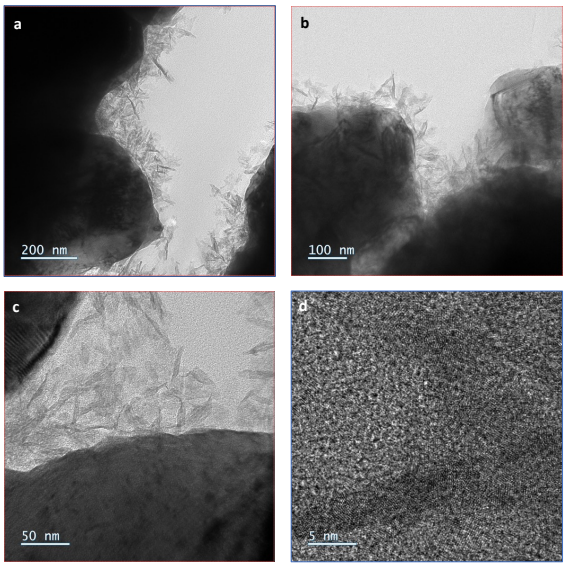

Figure S3. High resolution TEM imaging of porous Ni/MnO_2 electrode showing flaky deposits of ramsdellite MnO_2. Magnification: a) x 30k. b) x 40k. c) x 100k. d) x 800k.

a

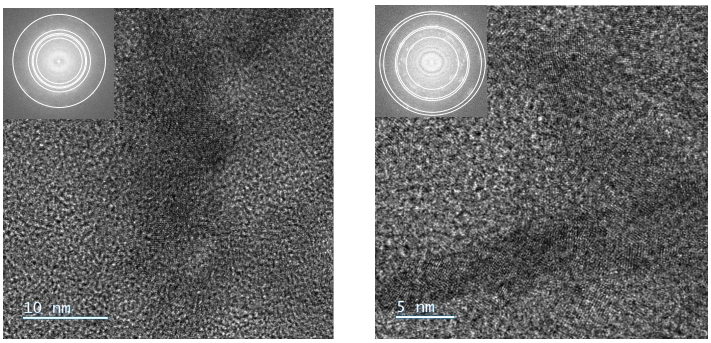

b

d_{TEM} (nm)	d_{ICSD} (nm)	hkl	% error
0.1200	0.1210	0 2 2	0.8 %
0.1258	0.1264	4 0 3	0.5 %
0.1732	0.1742	1 1 2	0.6 %
0.1821	0.1825	3 0 2	0.2 %
0.1715	0.1716	5 0 1	0 %
0.1913	0.1905	3 1 1	0.4 %
0.2371	0.2341	1 1 1	1.2 %
0.2058	0.2063	4 0 1	0.3 %
0.2265	0.2261	0 0 2	0.2 %
0.1256	0.1249	3 2 1	0.5 %
0.2308	0.2318	4 0 0	0.5 %
0.2562	0.2552	3 0 1	0.4 %

Figure S4. Comparison of interplanar spacings deduced from FFT of HR-TEM images with ramsdellite-MnO_2 *hkl*. a) HR-TEM digitized image at different magnifications and corresponding reduced FFT (inset). b) Comparison of interplanar spacing from FFT analysis, d_{TEM}, and reference data of MnO_2 ramsdellite taken from the Inorganic Crystal Structure Database (ICSD), d_{ICSD}. Interplanar spacings of ramsdellite-MnO_2 are clearly identified with mismatch errors below 1.2 %.

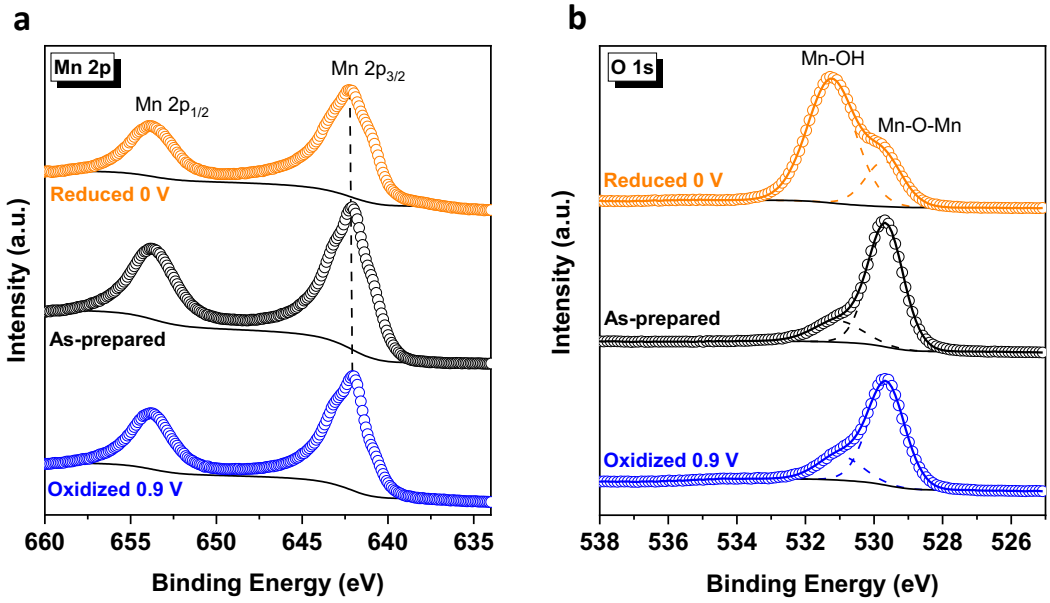

Figure S5. XPS spectra of reduced and oxidized manganese oxide. a) Mn-2p core-level. b) O-1s core-level.

The peak separation between the Mn-$2p_{3/2}$ and the lower binding energy component of the O-1s can be used to determine the mean oxidation of Mn[*]. This approach is consistent with a high Mn(IV) content in our oxidized material (Δ_{Mn-O} value of 112.4 eV).

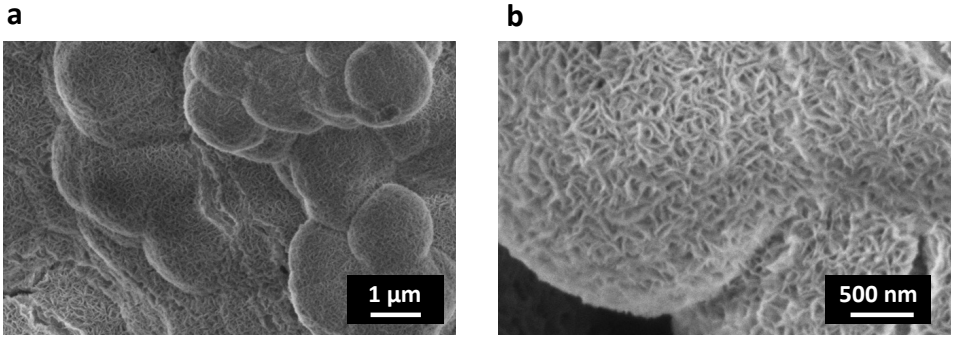

Figure S6. SEM image of a Ni DHBT/MnO_2 electrode after long cycling tests. a) Low magnification. b) High magnification showing the preservation of the MnO_2 nanoflakes.

[*] M. Toupin, T. Brousse, D. Bélanger, Influence of microstructure on the charge storage properties of chemically synthesized manganese dioxide. Chem. Mater. 14 (2002) 3946-3952.

Supplementary Material

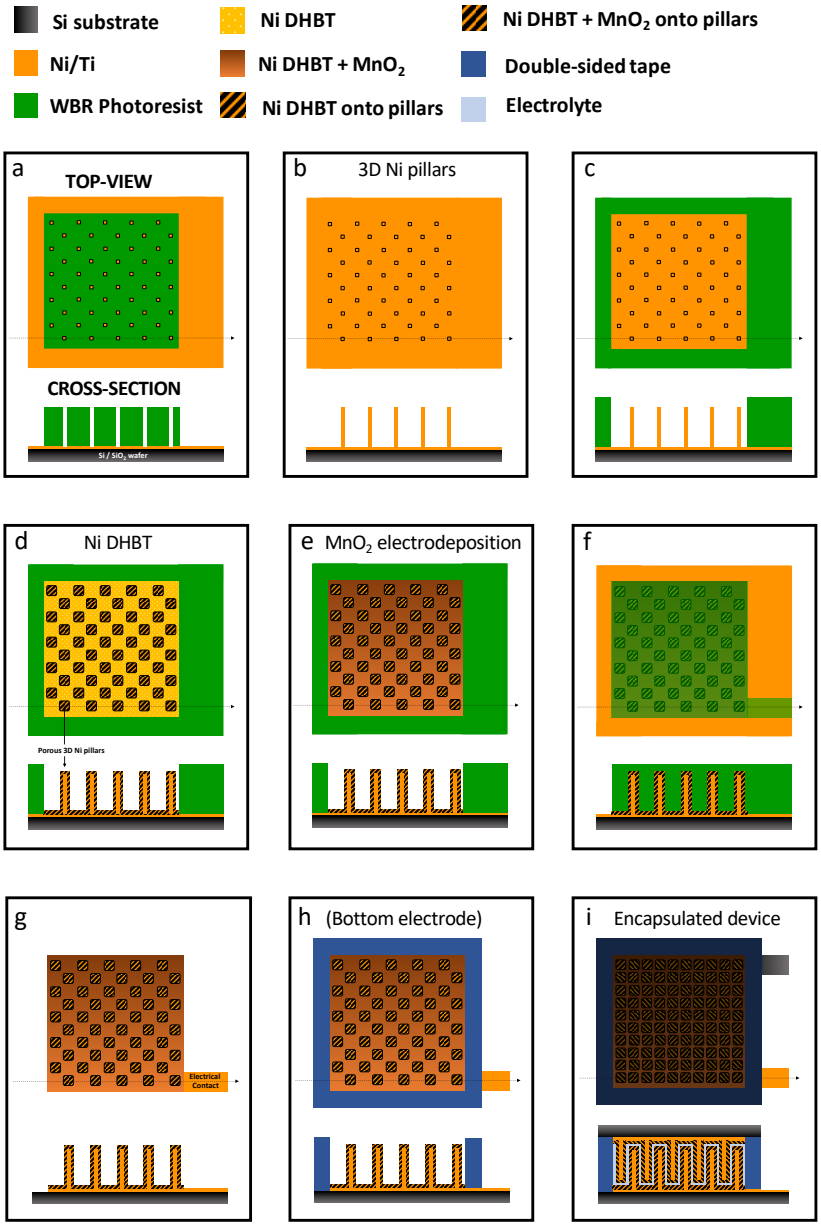

Figure S7. Microfabrication of micro-supercapacitors based on 3D entangled pillars: top-view and cross-section schematics of the different processing steps. a) Deposition and patterning using conventional photolithography techniques of a thick WBR photoresist on an oxidized silicon wafer coated with a thin Ti/Ni sublayer. b) Electrodeposition of Ni inside photoresist molds to obtain Ni pillars after WBR stripping. c) Design of square electrode area using a 400 µm-thick WBR photoresist. d) Uniform electrodeposition of porous Ni using the DHBT technique on the exposed surface (flat surface and pillars). e) Pulsed electrodeposition of MnO_2 on DHBT Ni. f) Protection of electrode area and electrical contact pads by a sacrificial WBR photoresist. g) Wet etching of the exposed Ni flat surface. h) Application of a double-sided self-adhesive tape (Tesa® chemical resistant filmic tape) on the first electrode to form a cavity. i) Filling of the cavity with electrolyte and final assembly of the two electrodes by controlled adjustment of the interspacing.

Supplementary Material

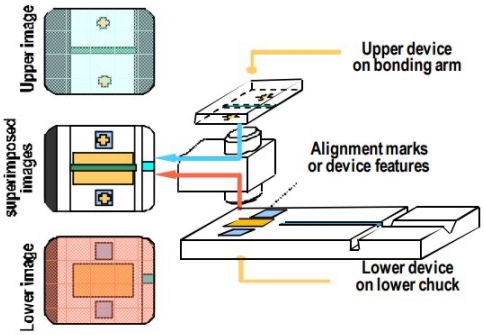

Figure S8. Assembling details. The FC150 - FlipChip Bonder equipment was used to assemble the interdigitated device with a precision of ± 1 µm by following the steps below:

1. The upper electrode is placed face down onto the bonding arm.
2. The lower electrode (containing the cavity formed by the tape and filled with electrolyte) is loaded onto the lower chuck.
3. The alignment marks of the lower electrode are centered using upper and lower lenses of the optics, in the field of view of the upper electrode, by moving the chuck horizontally.
4. The bonding arm moves vertically to contact the upper electrode with lower electrode.
5. A force of 1 kg is applied to stack the upper and lower electrode.

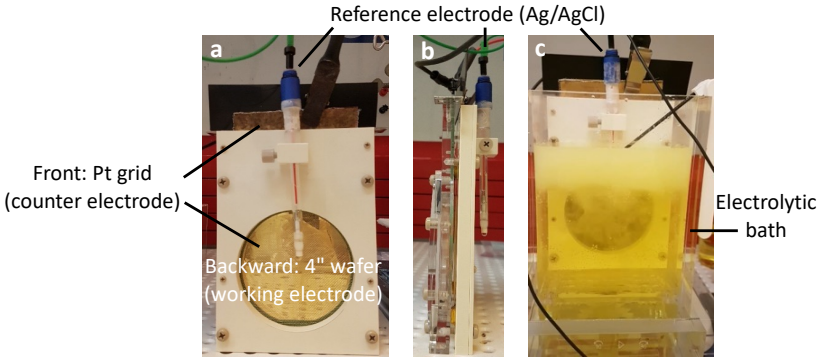

Figure S9. Electrochemical cell dedicated for 4-inch substrates for large-scale electrolytic deposition of the porous current collector and active material. a) Front view. b) Side view. c) Immersed in the deposition bath. The custom-made cell was designed in collaboration with Yamamoto-MS.

Supplementary Material

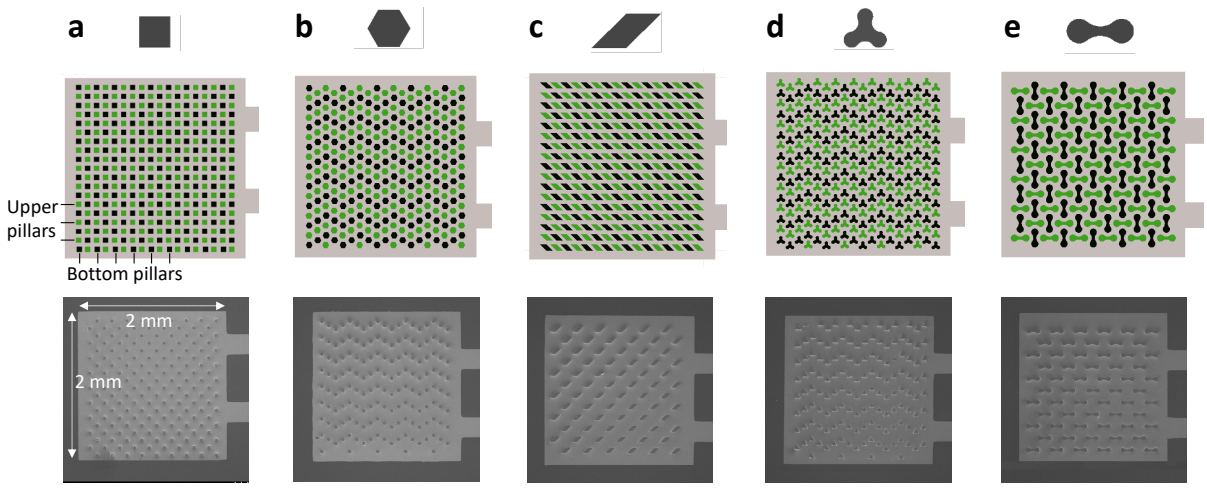

Figure S10. 3D pillar design illustrations. Mask design (2D projection of the two electrodes after assembly) with: a) Square pillars. b) Hexagonal pillars. c) Parallelogram pillars. d) Spinner pillars. e) Dumbbell pillars. SEM images: Top-view of a single electrode (2 x 2 mm^2).

The size, shape, height and density of the pillars on a given surface can be easily adjusted to optimize *3D Gain*, defined as the ratio between the exposed surface including all the pillars, S_{3D}, and the exposed surface without pillars, S_{2D}. Table S1 shows some examples of pillar topology on a S_{2D} = 4 mm^2 surface.

S_{unit} = 25980 µm²	Square 1	Hexagonal 1	Parallelogram 1	Spinner 1	Dumbbell 1
P_{unit} (µm)	644	600	777	774	805
Density / electrode	36	36	36	36	32
3D Gain	2.2	2.1	2.4	2.4	2.3

S_{unit} = 9353 µm²	Square 2	Hexagonal 2	Parallelogram 2	Spinner 2	Dumbbell 2
P_{unit} (µm)	386.8	360	466.9	467.5	482.5
Density / electrode	78	75	72	75	72
3D Gain	2.5	2.4	2.7	2.8	2.7

	Square 3	Hexagonal 3	Parallelogram 3	Spinner 3	Dumbbell 3
S_{unit} (µm²)	3600	4157	4900	4470	12334
P_{unit} (µm)	240	240	240	326.1	545.4
Density / electrode	171	157	136	144	60
3D Gain	3.1	2.9	2.6	3.4	2.6

Table S1. Surface gain for different geometric shapes and sizes of the pillars. S_{unit} and P_{unit}: base surface and perimeter of a single pillar, respectively. *Density / electrode*: number of pillars per electrode (cell size 4 mm^2). *3D Gain* is calculated for a pillar thickness of 200 µm.

Supplementary Material

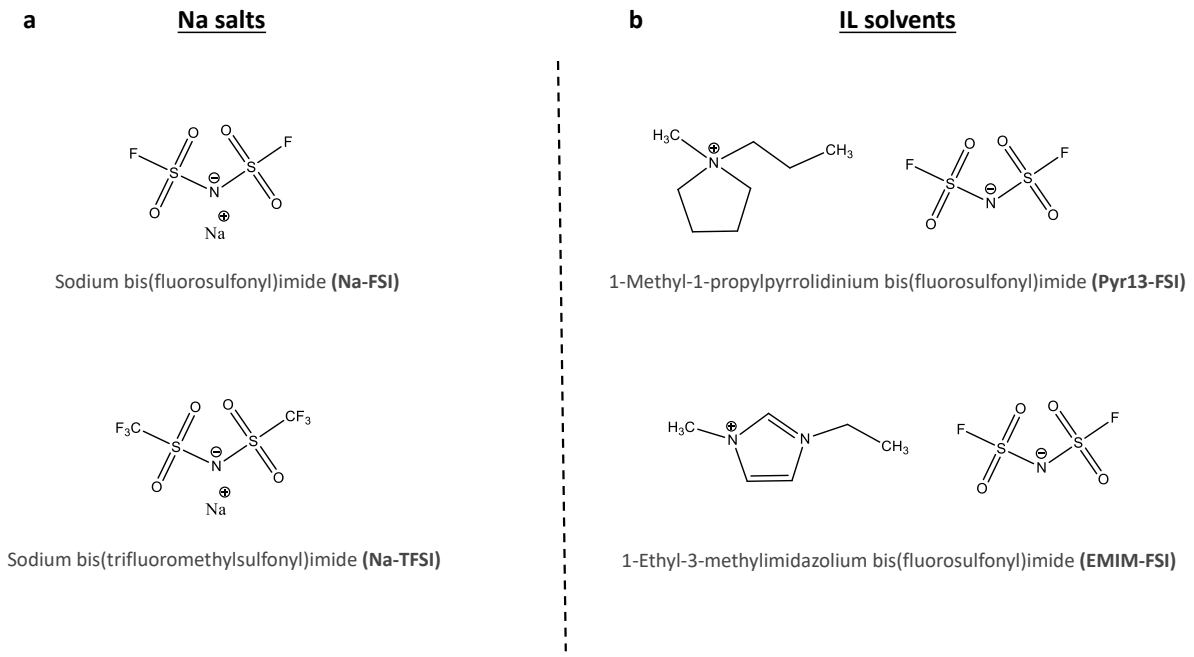

Figure S11. Structures of the cation and anion groups of ionic liquid candidates explored for MnO_2 micro-supercapacitors. a) Na salts. b) Ionic liquids solvents.

The comparison between NaFSI and NaTFSI was to evaluate if the transport of ions (and viscosity) has an impact on the charge storage properties. FSI^- anions provides higher conductivities from the better mobility of the smaller ion.
Regarding the EMIM-FSI and Pyr_{13}-FSI solvents, they were chosen for their relatively low viscosity (25 and 53 cP, respectively). $EMIM^+$ cation has better transport properties but is less stable at lower potential values because of the acidity of the proton at the C2 position (the carbon between both N on the cycle). Pyr_{13}^+ cation has been applied with more success as battery electrolyte[†] since the absence of acidic protons and of conjugation on the cycle decreases the reactivity.

[†] X. Wang, M. Salari, D. Jiang, J.C. Varela, B. Anasori, D.J. Wesolowski, S. Dai, M.W. Grinstaff, Y. Gogotsi, Electrode material-ionic liquid coupling for electrochemical energy storage. Nat. Rev. Mater. 5 (2020) 787-808.

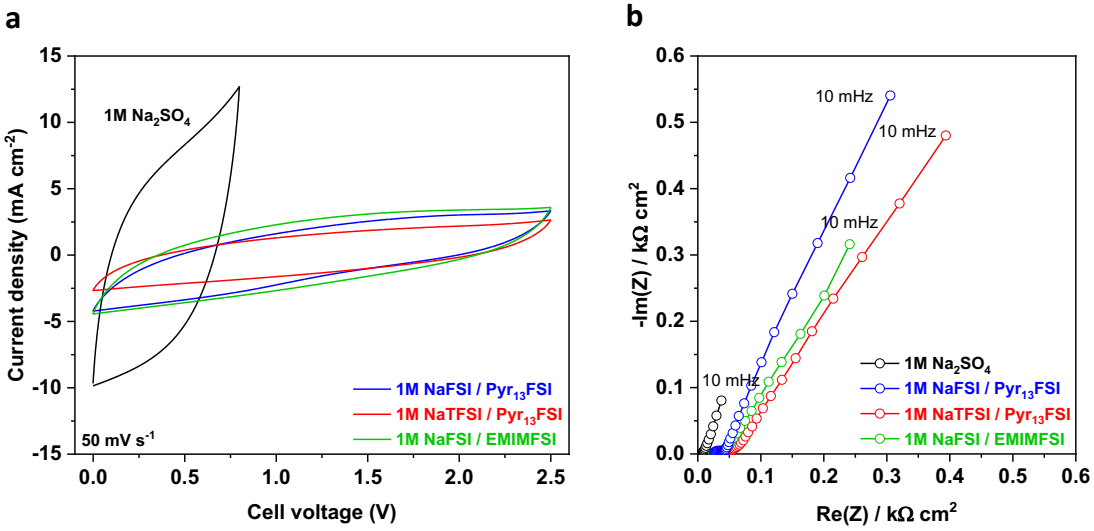

Figure S12. Electrochemical supercapacitor behaviour in Na salts-based ionic liquids using very thin film of Ni / MnO_2 electrodes (5 min Ni DHBT + 1000 cycles of MnO_2). a) Cyclic voltammogram recorded at 50 mV s^{-1} up to 2.5 V. b) EIS characteristics from 100 kHz to 10 mHz.

No significant difference is observed between the different investigated ionic liquids on the performances (power rating and cell voltage) of the MnO_2 micro-supercapacitor. The limitations seem therefore to come from interfacial reactions and/or ion transport within the active material, rather than ion transport within the electrolyte itself. Moreover, the potential limits do not appear to be too stringent for $EMIM^+$ cation (*i.e.* the negative limit is not negative enough for $EMIM^+$ to react) for a difference to be observed with the Pyr_{13}^+.

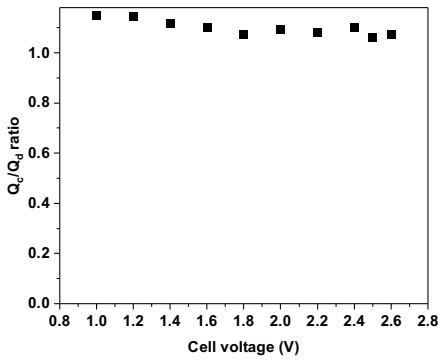

Figure S13. Voltammetric charge/discharge ratio Q_c/Q_d with increasing cell voltage in 1 M NaFSI /Pyr_{13}FSI computed from Fig. 3d. The charge/discharge ratio is constant from 1 to 2.6 V, indicating appreciable level of stability of the micro-supercapacitor within this voltage range [‡,§]

[‡] K. Xu, S.P. Ding, T.R. Jow, Toward reliable values of electrochemical stability limits for electrolytes. J. Electrochem. Soc. 146 (1999) 4172-4178.
[§] D. Weingarth, H. Hoh, A. Foelske-Schmitz, A. Wokaun, R. Kötz, A reliable determination method of stability limits for electrochemical double layer capacitors. Electrochim. Acta 103 (2013) 119-124.

Supplementary Material

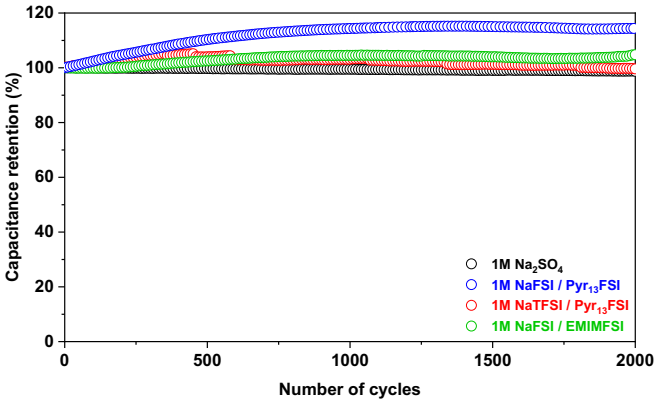

Figure S14. Long-term cycling performance of porous Ni/MnO_2 micro-supercapacitor cells in various ionic liquid-based electrolytes. 1 M Na_2SO_4 and 1 M NaFSI / $Pyr_{13}FSI$ were tested using a 179 µm thick Ni / MnO_2 electrodes. 1 M NaTFSI / $Pyr_{13}FSI$ and 1 M NaFSI / EMIMFSI were tested using a thin film of Ni / MnO_2 electrodes (5 min Ni DHBT + 1000 cycles of MnO_2).

Electrode material	Electrolyte	Areal Energy	Areal Power	Ref.
Graphene	1 M H_2SO_4	0.1 to 0.6 µWh cm^{-2}	2.2 to 10.8 mW cm^{-2}	[52]
VN	1 M KOH	0.5 to 1.9 µWh cm^{-2}	0.2 to 10.0 mW cm^{-2}	[53]
Carbon onions	1 M Et_4NBF_4 in PC*	0.4 to 1.2 µWh cm^{-2}	27.9 to 202.9 mW cm^{-2}	[51]
Carbide-derived carbon	1 M H_2SO_4	0.9 to 1.6 µWh cm^{-2}	0.3 to 32.5 mW cm^{-2}	[23]
3D MnO_2	EMIM-TFSI*	3.7 to 6.1 µWh cm^{-2}	0.1 to 7.6 mW cm^{-2}	[17]
3D PEDOT*	LiCl in PVA*	5.4 to 6.0 µWh cm^{-2}	0.04 to 2.0 mW cm^{-2}	[37]
Activated carbon	1 M Et_4NBF_4 in PC*	4.3 to 11.1 µWh cm^{-2}	2.7 to 20.8 mW cm^{-2}	[51]
3D RuO_2	0.5 M H_2SO_4	0.03 to 0.08 mWh cm^{-2}	0.1 to 13.8 mW cm^{-2}	[54]
3D MnO_2	1 M Na_2SO_4	0.04 to 0.08 mWh cm^{-2}	0.3 to 8.1 mW cm^{-2}	This work
3D MnO_2	1 M NaFSI in $Pyr_{13}FSI$	0.08 to 0.3 mWh cm^{-2}	0.9 to 11.1 mW cm^{-2}	This work

**PC: propylene carbonate, PEDOT: poly(3,4-ethylenedioxythiophene), PVA: poly(vinyl alcohol), EMIM-TFSI: 1-ethyl-3-methylimidazolium bis(trifluoromethylsulfonyl)imide.*

Table S2. Performance table with state-of-the-art micro-supercapacitors.